Sustainable Energy & Fuels

# Cooperative Effects of Surface and Interface Treatments in Hematite ($\alpha$-$Fe_2O_3$) Photo-Anode on Its Photo-Electrochemical Performance



| | |
|---|---|
| Journal: | *Sustainable Energy & Fuels* |
| Manuscript ID | SE-ART-11-2019-001081.R2 |
| Article Type: | Paper |
| Date Submitted by the Author: | 29-Dec-2019 |
| Complete List of Authors: | Inaba, Mika; Chuo University, Department of Applied Chemistry<br>Katayama, Kenji; Chuo University, Department of Chemistry; Kagaku Gijutsu Shinko Kiko, Precursory Research for Embryonic Science and Technology<br>Sohn, Woon Yong; Chuo University, Department of Applied Chemistry |
| | |

# Cooperative Effects of Surface and Interface Treatments in Hematite ($\alpha$-$Fe_2O_3$) Photo-Anode on Its Photo-Electrochemical Performance

Mika Inaba[1], Kenji Katayama[1,2] and Woon Yong Sohn[1]*

*1. Department of Applied Chemistry, Faculty of Science and Technology, Chuo University, 1-13-27 Kasuga, Bunkyo, Tokyo 112-8551, Japan*

*2. JST, PRESTO, 4-1-8 Honcho, Kawaguchi, Saitama, 332-0012, Japan*

*Corresponding author:

W. Y. Sohn, Phone: +81-3-3817-1899, E-mail: nunyong@kc.chuo-u.ac.jp

**Abstract**

To enhance the efficiency of the oxygen evolution reaction of hematite ($\alpha$-$Fe_2O_3$), we engineered both the surface of the hematite nanorods and the FTO/hematite interface simultaneously with an optimal annealing condition. We demonstrated that the enhancement of the photo-electrochemical performance of the hematite film treated by

both methods was not just the summation of the improvements originating from each treatment but showed a significant cooperative effect. We clearly revealed that the strong electric field was effectively induced by the surface P doping with the concentration gradient profile, resulting in the band bending even at 0 V vs RHE. Furthermore, the dead layer was removed by the $TiO_2$ underlayer, giving rise to Fermi level unpinning. We confirmed that the introduction of the $TiO_2$ underlayer unpinning Fermi level enables to build on the strength of the intrinsic long-lived holes generated by P doping, which is the origin of the cooperative effect.

**Keywords**: hematite, photo-electrochemical cell, water splitting, titanium dioxide, doping, phosphorus, time-resolved spectroscopy

## 1. Introduction

In 2016, the member countries of United Nations (UN) set the Sustainable Development Goals (SDGs) and one of them was to ensure access to affordable, reliable, sustainable and modern energy for all. Because the amount of fossil fuels in our earth are limited and burning of fossil fuels inevitably causes serious environmental pollution, humanity cannot permanently use fossil fuels. Thus, as UN decided, finding

the alternative energy sources for replacing fossil fuels is one of the urgent issues facing the human race today.

There are many attempts for the development of new alternative energy sources and one of them is to use sunlight streaming toward earth for the production of hydrogen gas by splitting water. For example, $H_2$ production via solar water splitting using photoelectrochemical (PEC) cells has been attracting a lot of attentions as an effective way to generate the clean energy source. This idea has been realized since Fujishima and Honda succeeded in demonstrating the light-induced water splitting with a $TiO_2$ photo-anode and a Pt counter electrode for the first time.[1]

In order to achieve the effective water splitting using the PEC cell, multiple physical and chemical properties of the photo-electrode material must be taken into account such as strong visible-light absorption, appropriate conduction and valence band positions, efficient charge separation and transport/transfer kinetics.[2-4] Apart from $TiO_2$, several kinds of semiconductor materials have been developed to be utilized for the photo-electrode in the PEC cell[5-14] and hematite ($\alpha$-$Fe_2O_3$) has been regarded as one of the best photo-anode materials because this material well satisfy the above mentioned conditions.[15-17] However, it also has various limiting factors such as poor conductivity[4], short hole diffusion length[18, 19], strong recombination[20-22] and slow oxygen-evolution

kinetics,[23, 24] which must be improved for its implementation. In order to address these problems, several approaches (e.g. nanostructured architecture[25-27], surface modification[3, 28-30], and introduction of impurities[31, 32] have been reported. Among these techniques, the doping, introduction of the impurities into the target material, has attracted many attentions as a powerful approach to overcome the above mentioned problems of hematite because it could potentially increase both carrier concentration and mobility, leading to the enhancement of the conductivity in the hematite film.[33]

In many cases, dopants were incorporated into the crystal lattice of hematite uniformly during the fabrication process of hematite, called bulk doping, such as hydrothermal growth, electro-deposition, chemical vapor deposition and atomic layer deposition,[25, 34, 35] influencing mainly bulk states.[36] Even though it has been reported that this method could improve the conductivity of the photo-excited charge carriers, the effect is not so significant because of the generation of the deep trap states in the bulk, inhibiting the charge diffusion. On the other hand, surface doping, such as a wet impregnation method in which the dopants are dispersed into the surface and/or new heterogeneous metal oxides phases are produced on the surface during calcination at high temperature,[36-38] could form the depletion region generated by the impurities at the surface, resulting in the improvement of the charge mobility and the charge separation

efficiency.[37] Moreover, Luo et al. demonstrated that this effect could become increasingly greater by increase in the concentration gradient effect of the impurities. They reported that this method named gradient doping drastically improved the PEC performance by optimizing temperature and the duration of the annealing process with an aid of the enhanced charge separation resulting from widening the depletion region.[39-40]

In addition, in order to achieve the high PEC performance of hematite, the lattice mismatch between the tin oxide in fluorine-doped tin oxide (FTO) substrate and the hematite film, generating a "dead layer", must be taken into account.[41-44] It has been reported that the strong interactions between the hematite film and the FTO substrate produce intermediate defect states, acting as recombination centers and causing Fermi level pinning.[44] In order to solve this problem, introducing an interlayer between the FTO substrate and the hematite film could be a proper way to remove the dead layer. Furthermore, the underlayer could play various roles in not only removing the dead layer but also providing the dopant source, which could be realized by controlling the annealing temperature. According to a former study reported by Luo Z et al., in the presence of the $TiO_2$ underlayer, the photocurrent of a hematite film was improved, which was attributed to the alleviation of the lattice mismatch between hematite and the

FTO substrate when the hematite film was sintered at low temperature ( ~550 °C).[27] On the other hands, when it was calcined at higher temperature, the crystallinity of hematite was improved and the $Ti^{4+}$ dopant was introduced from the $TiO_2$ interlayer, which enhanced the conductivity of the hematite film.[27] Several metal oxide underlayers such as $ZrO_2$[45], $Nb_2O_2$[46], $SiO_x$[46] and $TiO_2$[46-48] have been explored and it was demonstrated that the PEC performance of hematite could be enhanced by introducing one of them into the FTO/hematite interface with aids of the above mentioned effects.

Likewise, the effects of each treatment on the surface of hematite and the FTO/hematite interface have been well understood but the comprehensive influences arising from both treatments have not been investigated yet. Therefore, in this study, we engineered both the surface of the hematite nanorods with P doping and the FTO/hematite interface with the $TiO_2$ underlayer using a simple and easy solution-based method with an optimal annealing condition, in which the $TiO_2$ underlayer not only reduced the lattice mismatch but also provided the Ti dopant from the underlayer to the inside of the hematite nanorods. In addition, in order to effectively incorporate the dopants into the hematite nanorods and also expand the depletion layer, we employed a very short and high temperature annealing process, which is the gradient doping. Because of the cooperative effects of those treatments, the fabricated film showed a

drastic improvement of the PEC performance. Furthermore, in order to reveal the effect of each treatment on the photo-excited charge carrier kinetics, we employed a time-resolved spectroscopic technique and clearly demonstrated the role of each treatment in the physical and chemical properties of hematite by studying the charge carrier dynamics.

## 2. Experimental

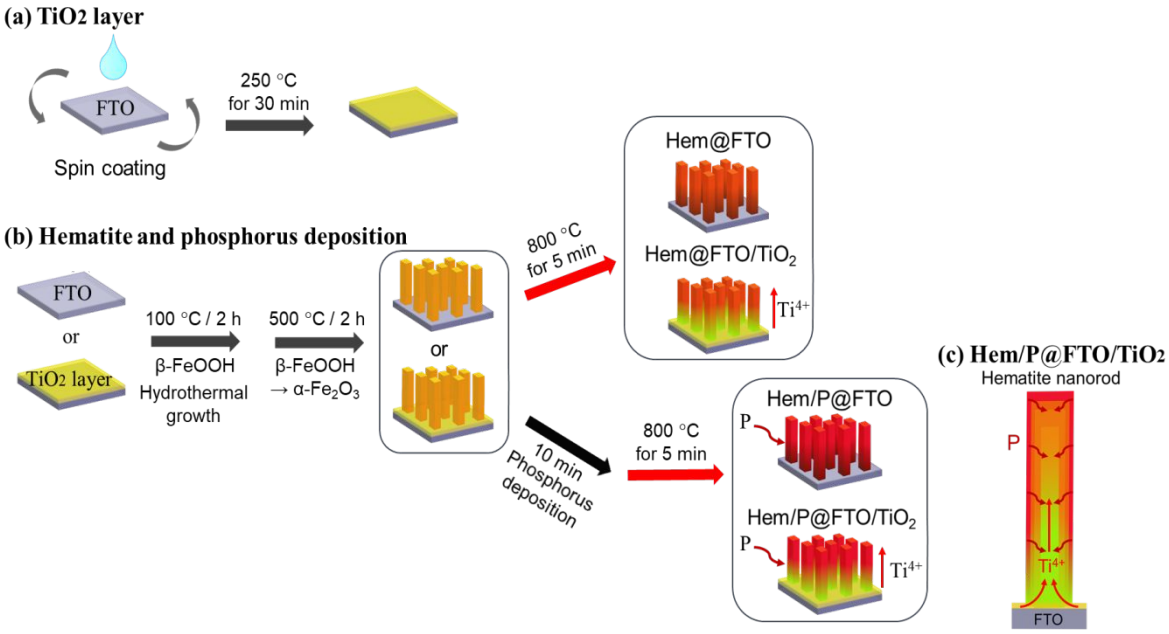


Scheme 1 Schematic diagram of the experimental procedure of (a) deposition of $TiO_2$ underlayer and (b) hematite deposition and phosphorus incorporation and (c) cross-section schematic diagram of a single nanorod in Hem/P@FTO/$TiO_2$

### $TiO_2$ interlayer synthesis

Titanium precursor solution, 0.15 M titanium diisopropoxide bis(acetylacetate) (75

wt% in isopropanol, Aldrich) in 1-butanol was deposited on the FTO substrate (~7 Ω/sq, SOLARONIX) by spin coating (1500 rpm for 30 sec) and then heated at 250 °C for 30 min[47] as shown in Scheme 1(a).

**Hematite synthesis**

In this study, we fabricated hematite films, based on a solution derived method that was described in previous reports,[13, 21, 49, 50] as shown in Scheme 1(b). Briefly, at first, FTO or $TiO_2$/FTO were vertically aligned in solution consisting of 0.3 M iron (III) chloride hexahydrate ($FeCl_3$, 99.9 %, Wako) and 2 M sodium nitrate ($NaNO_3$, 99.9 %, Wako). The solution was acidified by 0.19 mL Hydrochloric acid (HCl, 20.0%, Wako) to prevent iron precipitation.[51] Deposition reaction was carried out at 100 °C for 2 h (Hydrothermal growth). After cooling down to room temperature, the samples were rinsed with deionized water. Color of the FTO substrate became yellow because of the formation of β-FeOOH on the FTO substrate. The samples were annealed at 500 °C for 2 h and a ramp rate of 10 °C/min to convert β-FeOOH into hematite. The bare hematite film and the film including the $TiO_2$ interlayer are denoted as Hem@FTO and Hem@FTO/$TiO_2$, respectively. For the phosphorus incorporation, Hem@FTO and Hem@FTO/$TiO_2$ were soaked in 0.2M $Na_3PO_4$ (Wako) solution for 10 min and the

films were dried in a furnace at 100 °C for 1.5 h.[39] (denoted as Hem/P@FTO and Hem/P@FTO/$TiO_2$, respectively) Finally, the as-prepared samples (Hem@FTO, Hem@FTO/$TiO_2$, Hem/P@FTO, Hem/P@FTO/$TiO_2$) were calcined at 800 °C for 5 min to induce the introduction of the impurities as shown in Scheme 1(b) and (c), and then washed the surface with DI water.

**Characterization**

The nanostructure of a hematite single rod was examined by scanning electron microscopy (SEM, HITACHI, S-5500, 3 kV) and bright field scanning transmission electron microscopy (BF-STEM, HITACHI, S-5500, 10 kV). In order to observe the single rod, the hematite film deposited on the FTO substrate was scrapped out, and then dispersed in 2 ml acetone (Wako). This suspension was dropped on a collodion-coated copper grid and dried under vacuum. The surface morphologies of the hematite films were observed by scanning electron microscope (SEM, HITACHI, S-4300). X-ray diffraction (XRD) spectra of the hematite films were measured by X-ray diffractometer (Rigaku, MiniFlex 600). The element compositions in the as-prepared samples, derived from the binding energies of the electrons, were examined by X-ray photoelectron spectrometer (Kratos, AXIS-HSi).

**PEC measurements**

The current densities as a function of the applied bias voltage of the PEC cell consisting of the as-prepared hematite film (working electrode), a Pt counter electrode and a reference electrode (Ag/AgCl/Saturated KCl) were measured in KOH aqueous solution (pH 11.9). Linear sweep voltammetry (LSV) was performed using potentiostat analyzer (EC FRONTIER, ECstat-100) either in dark or under AM 1.5 G light (100 $mW/cm^2$) and the electrolyte solution was purged with Ar gas for 30 min before measuring LSV. All the applied potential values (vs Ag/AgCl), reported in this work, were converted into the corresponding values (vs RHE) using the Nernst equation,

$$E_{RHE} = E_{Ag/AgCl} + 0.059\text{pH} + E^0_{Ag/AgCl}$$

, where $E^0_{Ag/AgCl}$ is 0.198 at 25 °C.

**Time-resolved measurements**

In order to investigate the photo-excited charge carrier kinetics, a heterodyne transient grating (HD-TG) technique which is one of the time-resolved spectroscopic techniques and sensitive to the dipole change at the solid/liquid interface was employed.[21, 49, 50, 52-54] The second harmonic output of a Nd:YAG (YAG) laser (532 nm, 0.2−0.5 mJ/pulse, 10 Hz, pulse width: 5 ns) and a semiconductor laser (638 nm) were used as

pump and probe lasers, respectively, to prevent the unintended simultaneous excitation from the $TiO_2$ underlayer. The grating space used in the present work was 70 μm. The target was excited by the pump irradiation, generating the transient grating on the sample, and the response was measured via the diffraction of the probe light. The signal was detected by a photodiode (Thorlabs, DET110, rise time: 14 ns) and amplified by a voltage amplifier (Femto, DHPVA). To eliminate the scattered pump light entering the detector, a filter for cutting 532 nm and a long pass filter (>550 nm) were also placed in front of the entrance of the detector. It was monitored and recorded by an oscilloscope (Agilent, DSO8104A, 4GSa/s). In order to measure the HD-TG responses under the bias voltage condition, we built a PEC cell consisting of three electrodes; the hematite film as a working electrode, a Pt counter electrode, and a reference electrode (Ag/AgCl/Saturated KCl). They were placed into a quartz cell (3/Q/40, Starna Scientific) filled with an electrolyte solution (KOH, pH = 11.9). A potentiostat (HA-151B, Hokuto Denko) was employed to apply a bias voltage.

## 3. Results and discussion

Figure 1 shows the XRD patterns of all as-prepared samples. It was confirmed that the diffraction peaks labeled in Figure 1(a) correspond to the Bragg reflections from

the hematite (JCPDS 01-080-5413) and the $SnO_2$ rutile phases (JCPDS 01-079-6887) by taking into account the peak shift induced by the FTO substrate, shown in Figure S1 in Supplementary Information (SI). No other peaks were observed, identifying the existence of a single-phase hematite layer on the FTO substrate. In addition, no shifts by introducing the impurities were observed as shown in Figure 1(b). It means that the dopants incorporated into the hematite film hardly influenced its crystal structure at all because of its small amount.

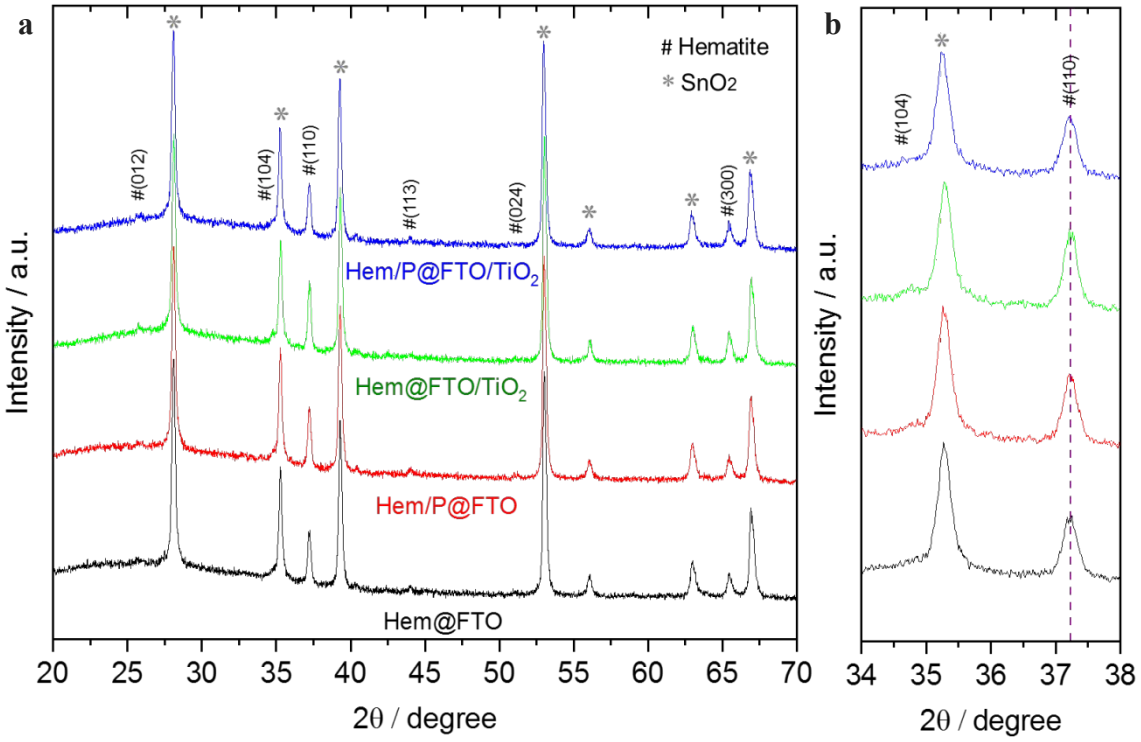


Figure 1 (a) X-ray diffraction patterns of Hem@FTO, Hem@FTO/$TiO_2$, Hem/P@FTO, and Hem/P@FTO/$TiO_2$, and (b) the magnified view in the vicinity of (110) and (104) peaks

The morphology of the hematite and the effect of the introduction of the impurities

on it were also examined by SEM (Figure 2 a-e). As can be seen in Figure 2a-d, each hematite film shows a nearly identical morphology, a nanorod shape, and it was more clearly identified by the EDX mapping as presented in Figure 2e and f. In the SEM images in Figure 2a-d, a remarkable difference was observed in Hem@FTO/$TiO_2$ and Hem/P@FTO/$TiO_2$, in which the hematite nanorods were more closely packed, compared to those in Hem@FTO and Hem/P@FTO, and it could be attributed to the different nucleation and growth mechanisms, resulting from the introduction of the $TiO_2$ underlayer.[47, 48, 55] The thickness of the hematite layer (350±10 nm) was also measured by the cross-section SEM images shown in Figure S2 in SI.

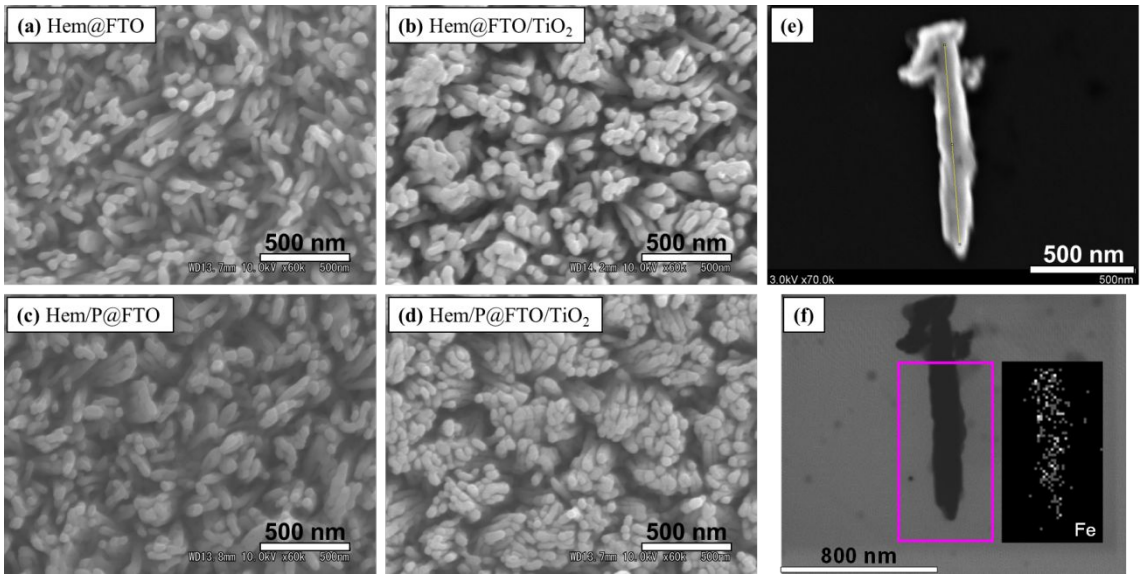


Figure 2 SEM top view of (a) Hem@FTO, (b) Hem@FTO/$TiO_2$, (c) Hem/P@FTO, and (d) Hem/P@FTO/$TiO_2$. (e) SEM image of a single hematite nanorod. (f) STEM image of a hematite nanorod shown in (e) and EDX mapping

In order to investigate light absorption properties of the as-prepared hematite films, UV-Vis absorption spectra were measured and presented in Figure S3 in SI. As shown

in the spectra, even though the absorption edge of all the hematite samples was observed at around 590 nm, it is noticeable that the treatments increased the absorption in the long wavelength range (600 nm), which could be attributed to the creation of the shallow impurity states in the treated hematite film.[56]

The concentration profiles of the impurities in the single rod of Hem/P@FTO/$TiO_2$ were examined by a point scan of EDX and presented in Figure 3 and S4 in SI. As shown in Figure 3d, it was confirmed that the Ti element was incorporated into the hematite from the $TiO_2$ underlayer, based on the higher concentration of Ti in the bottom than in the top. In addition, it was revealed that the P element was introduced into a hematite nanorod as shown in Figure 3d. Besides, it clearly shows the concentration gradient profile of P along the radial direction. These results support that the surface of hematite and the interface between the FTO substrate and the hematite film were successfully treated by each method.

Further investigation for revealing the effect of the P doping on the surface of the hematite film was performed by XPS. The presence of P at the surface in Hem/P@FTO was confirmed, based on the P 2p peak in the XPS spectra (Figure S5a in SI). The binding energy of P 2p in Hem/P@FTO was 133.1 eV, of which value is higher than that of elemental phosphorus (130.1 eV)[57] and similar to that of $FePO_4$ (133.4 eV). On

the other hand, the Fe 2p peaks in the XPS spectra (Fe $2p_{3/2}$: 710.9 eV and Fe $2p_{1/2}$: 724.4 eV) did not shift by introducing P at the surface (Figure S5b in SI). It means that no Fe-P bonds were created by the P doping on the surface in hematite, which enables the P elements to react with the lattice oxygen atoms, namely, locally reducing hematite. In addition, the O 1s peak in the spectra shows the decrease in the chemisorbed oxygen species (~532 eV) by the P doping on the surface in hematite (Figure S5c in SI), which supports the above result.

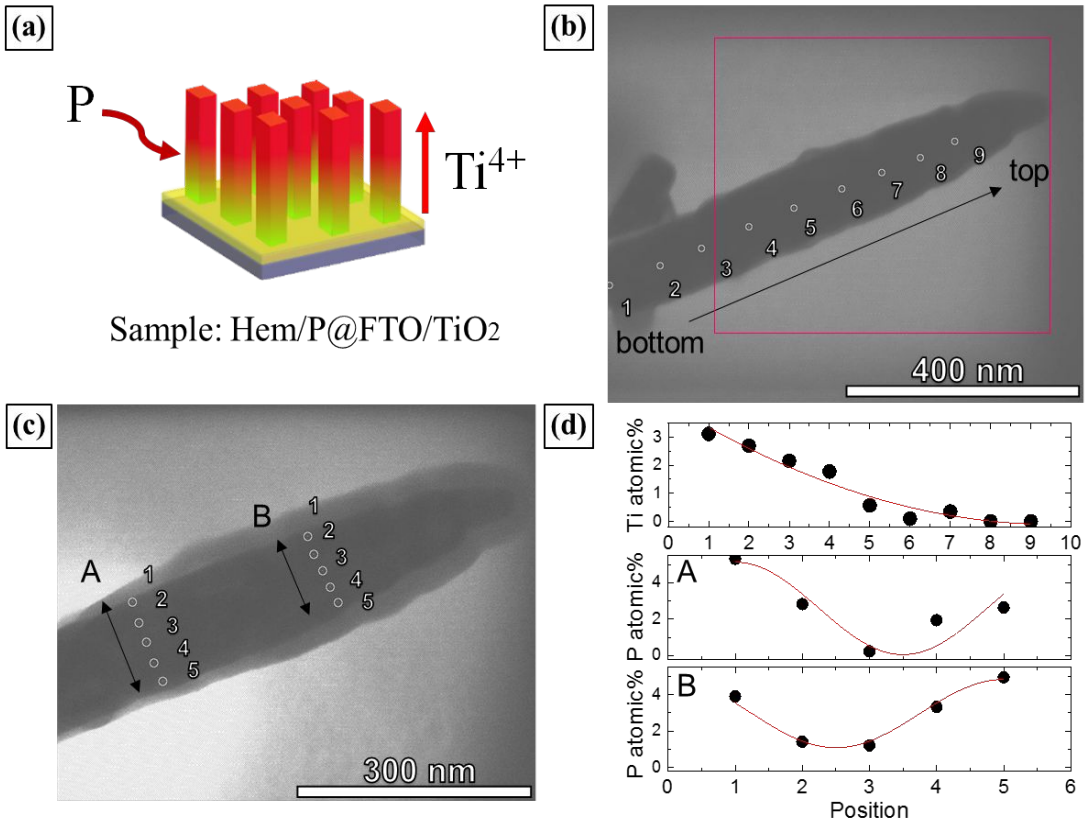


Figure 3 (a) Schematic illustration, (b) STEM image, (c) expanded STEM image and (d) Ti and P concentration profiles at each position in a single rod of Hem/P@FTO/$TiO_2$

The PEC performances of all the as-prepared samples were evaluated by measuring

the current densities as a function of the applied bias voltage, I-V curves, and presented in Figure 4. The photocurrent densities at 1.23V (vs RHE) were 0.10 mA/cm$^2$ (Hem@FTO), 0.12 mA/cm$^2$ (Hem@FTO/$TiO_2$), 0.15 mA/cm$^2$ (Hem/P@FTO), and 0.48 mA/cm$^2$ (Hem/P@FTO/$TiO_2$), respectively. These results clearly show that the introduction of either P on the surface or the $TiO_2$ underlayer just slightly enhanced the PEC performance of Hem@FTO, which was already reported in the previous study,[48] while the improvement was remarkable when both the surface and the interface were simultaneously treated. As can be seen in Figure 4, the photocurrent density of Hem/P@FTO/$TiO_2$ was approximately five times higher than that of bare hematite, Hem@FTO. Interestingly, the enhancement of the photocurrent density, resulting from the treatments of both the surface and the interface, was not just the summation of the improvement originating from each treatment but obviously showed a significant cooperative effect of the two methods on the performance. The detail of this phenomenon will be discussed later.

The dependence of the I-V curve of Hem/P@FTO/$TiO_2$ on the annealing temperature and the duration of the second calcination process is shown in Figure S6 in SI. As can be seen in the figure, the photocurrent density of each Hem/P@FTO/$TiO_2$ is obviously dependent on the second annealing condition. When the annealing condition

was 800 ºC/5 min (optimal condition), the current density at 1.23V (vs RHE) was higher than that of the hematite film, annealed at 750 ºC/10 min. Because of the high temperature of the optimal condition, the crystallinity of the hematite film was enhanced and the incorporations of the dopants from the $TiO_2$ underlayer and P at the surface were activated.[27] Besides, in this condition, P dopants were effectively introduced into the hematite film with the concentration gradient profile, leading to the generation of the strong electric field in the hematite film as mentioned above. On the other hand, longer or higher calcination temperature such as 800 ºC/10 min or 850 ºC/5 min resulted in the decrease in the current density due to the deformation of the hematite nanorod[27] or less effective dopant concentration profile. These indicate that the optimal condition of the second calcination process could lead to the balanced crystallinity, morphology, and dopant concentration profile.

In addition, we can expect that the electron transport efficiency in the $TiO_2$ underlayer could be improved by the $Ti^{4+}$-$Fe^{3+}$ exchanges, achieved by the second calcinations process, because it has been reported that the $Ti^{4+}$ in the $TiO_2$ underlayer could be substituted by $Fe^{3+}$ at high temperature, meaning that Fe doped $TiO_2$ could be generated in the underlayer, in accordance with former studies[58-61] and its current density is higher than that of the bare film with an aid of the reduction of the electron

transfer resistance.[61]

We also checked whether the high temperature of the annealing process could influence the conductivity of the FTO glass by measuring the resistances of the FTO substrates before and after the calcination and confirmed that the increase in the resistances was negligible (from 17.5 Ω/cm to 21.0 Ω/cm), which was due to the short annealing duration.

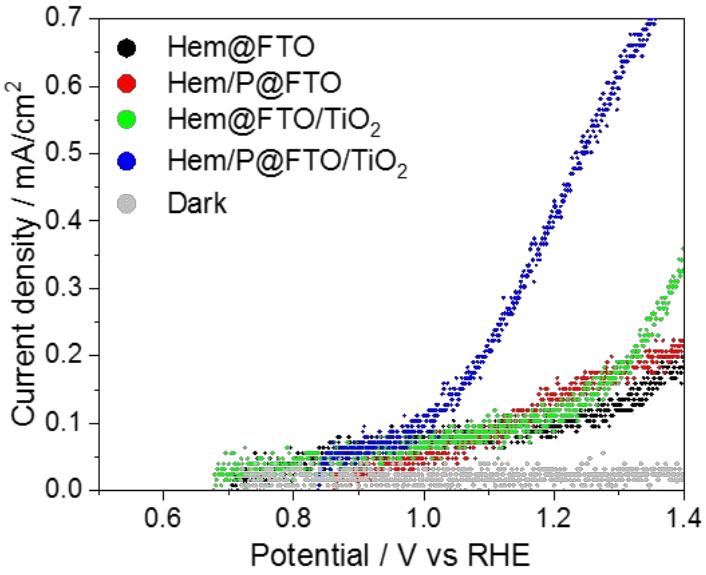


Figure 4 Photocurrent density-potential (I-V) curves of Hem@FTO (black), Hem/P@FTO (red), Hem@FTO/$TiO_2$ (green), and Hem/P@FTO/$TiO_2$ (blue)

In order to figure out the origin of the performance enhancement and the cooperative effect, realized by the treatments, we investigated the charge carrier kinetics of the as-prepared hematite films, ranging from microsecond to second, which is highly related to the water oxidation process, using the HD-TG method, one of the time-resolved spectroscopic techniques.[21, 49, 50, 52-54] It has been reported that most

photo-generated charge carriers decay within a few hundred nanosecond after the excitation event due to the ultrafast charge carrier recombination.[62] Thus, a transient absorption technique that is a conventional method to investigate the charge carrier dynamics shows potential weakness to study them in the slow timescale because, in this method, the absorption of the trapped charge carriers must be directly probed. In this respect, we selected the HD-TG technique which is sensitive to the dipole change at the solid/liquid interface[21, 49, 50, 52-54] to investigate the small number of the long-lived charge carriers, surviving at the surface in the hematite film, under a relatively low-intensity excitation condition, comparable to the solar irradiation. The principle of the HD-TG method is described in S6 in SI and its schematic diagram is shown in Figure S7 in SI.

The HD-TG responses of the as-prepared samples were measured in an aqueous solution, depending on the bias voltage, ranging from 3 μs to 1 s, and presented in Figure 5. It is very difficult to extract the exact time constants of each component because a sum of a large number of the exponential functions always generate a good fitting, distorting the results, called over-fitting. In order to overcome the difficulty to select an appropriate number of the exponential functions in the response consisting of multiple components arising from a variety of circumstances of the charge carriers, we

employed the maximum entropy method (MEM), enabling to yield a continuous distribution of lifetimes of discrete exponential responses by maximizing the data entropy using the noise amplitude as a prior information.[63] According to the result of the MEM analysis, all the observed responses included two decay components under the bias condition, which is consistent with the former works[21, 49, 62, 64] and the obtained time constants are listed in Table S1 in SI. The first decay component, appearing between $10^{-6}$ and $10^{-3}$ s, has been assigned to the recombination arising from the surface trapped holes ($\tau$ = 120 ~ 340 μs). In addition, the second component appearing from around $10^{-3}$ s corresponds to the charge transfer from hematite to electrolyte, originating from the long-lived holes ($\tau$ ~370 ms) and this assignment was clearly confirmed by the pioneer work conducted by Durrant and his co-workers.[62, 64] In these reports, they found that the signal amplitude of this component is quantitatively correlated with the photocurrent amplitude, meaning that the amount of the photo-excited charge carriers generating this component is directly related to the water oxidation reaction. Thus, based on the results, they concluded that this component arose from the long-lived holes trapped at the surface in the hematite film and the decay could be assigned to the charge transfer from hematite to electrolyte.[62, 64] Even though we cannot find the quantitative correlation between the signal intensity of the second component and the current density

shown in Figure 4 due to the differences of the wavelength and the type of light, we believe that the component we observed is same with what Durrant and his co-workers found and we can qualitatively discuss this in this study, based on the clear assignments in the former studies performed by ourselves.[21, 49, 52]

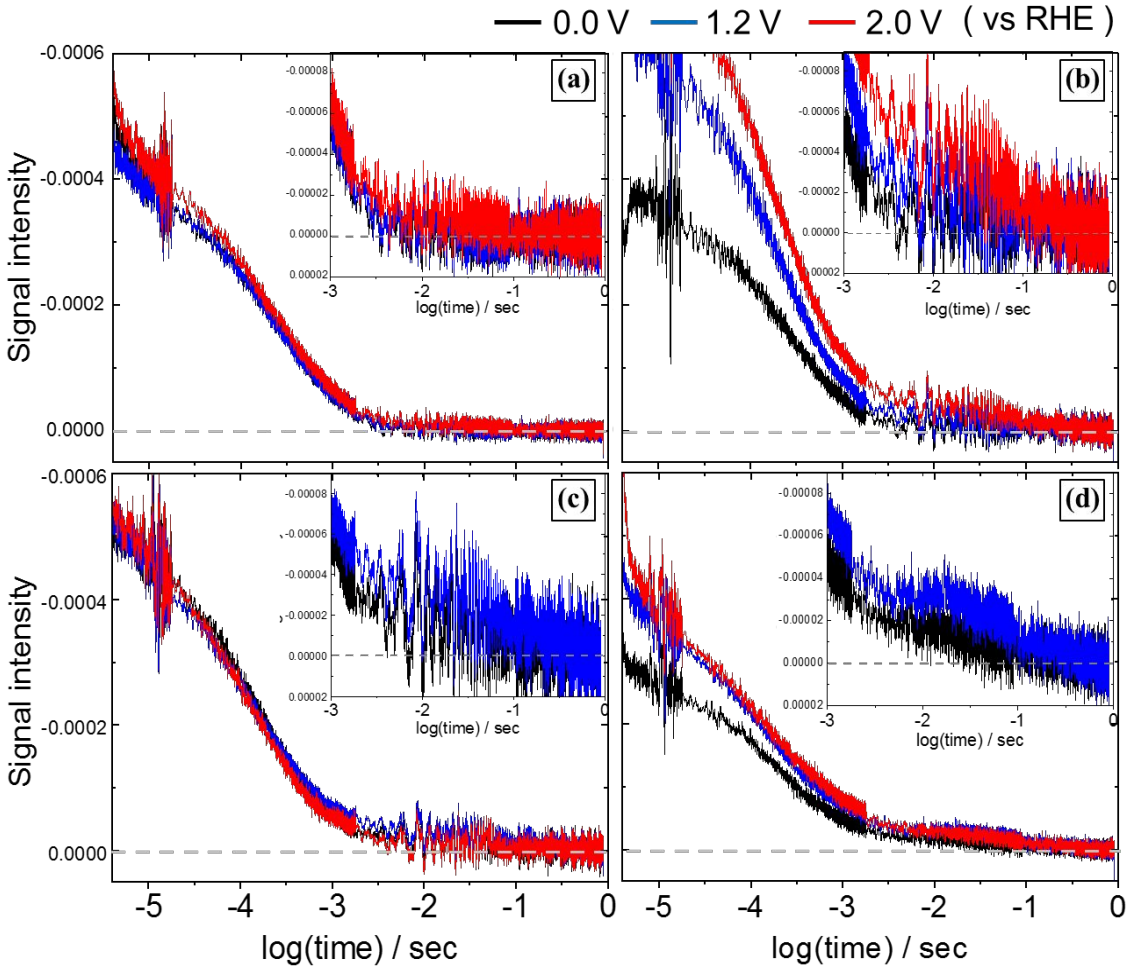


Figure 5 HD-TG responses of (a) Hem@FTO, (b) Hem@FTO/$TiO_2$, (c) Hem/P@FTO, (d) Hem/P@FTO/$TiO_2$ in aqueous solution, depending on the applied bias voltage, 0.00 V (black), 1.20 V (blue), and 2.00 V (red). Insets show the expanded TG responses ranging from millisecond to second.

As can be seen in Figure 5b, the signal intensities of both components significantly increased as an increase in the applied bias voltage in Hem@FTO/$TiO_2$, while

Hem@FTO and Hem/P@FTO exhibited the dependence on it very weakly (Figure 5a and c and S8 in SI). It means that the number of the photo-excited holes only in Hem@FTO/$TiO_2$ significantly increased under the bias condition because the band in it was bent by applying the bias voltage. Thus, it is obvious that the strong band bending under the bias condition resulted from the existence of the $TiO_2$ underlayer and it could be attributed to the removal of the dead layer by the underlayer, leading to Fermi level unpinning. With an aid of Fermi level unpinning realized by the $TiO_2$ underlayer, the space charge layer was significantly varied under the bias condition and charge carriers were well separated, resulting in the enhancement of the PEC performance shown in Figure 4. In addition, it is possible that the dead layer effect in a hematite was more alleviated by the Ti dopants from the $TiO_2$ underlayer as previously reported.[65]

In Figure 5c, as mentioned in the above paragraph, the signal intensities of both components in Hem/P@FTO depended on the applied bias voltage very weakly. However, even at 0 V vs RHE, as can be seen in the inset of Figure 5c, the second component clearly appeared, which implies that the impurity of P on the surface could generate the depletion layer at the surface in the hematite film, leading to the increase in the number of the long-lived holes. Furthermore, it has been reported that the electric field could be remarkably enhanced by the gradient doping treatment owing to the

production of more than one band bending region.[40] Thus, it is believed that the strong electric field was effectively induced by introducing P with the concentration gradient profile, resulting in the band bending even at 0 V vs RHE. However, the improvement of the PEC performance by introducing only P dopant was very small as can be seen in Figure 4. It means that it is necessary to add the external force that is the applied bias voltage to drive the oxygen evolution reaction using the long-lived holes, which was limited by Fermi level pinning resulting from the interface states in the dead layer in Hem/P@FTO.

In the case of Hem/P@FTO/$TiO_2$ where both treatments were applied, as shown in Figure 5d, the signal intensities of both components significantly increased as an increase in the applied bias voltage. In addition, the second component could be found without the applied bias voltage, which was observed in Hem/P@FTO. It means that Hem/P@FTO/$TiO_2$ has both advantages, unpinned Fermi level and the intrinsic depletion layer at the surface. As presented in the inset of the figure, the signal intensity of the second component arising from the long-lived holes was much larger than those in other cases, implying that the introduction of the $TiO_2$ underlayer unpinning Fermi level enables to build on the strength of the intrinsic long-lived holes generated by P doping. Consequently, applying both treatments in the surface and the interface

drastically improved the PEC performance cooperatively as shown in Figure 4.

The summary of the observed charge carrier kinetics in Hem/P@FTO/$TiO_2$ in comparison with that in Hem@FTO is shown in Figure 6. In all cases, the

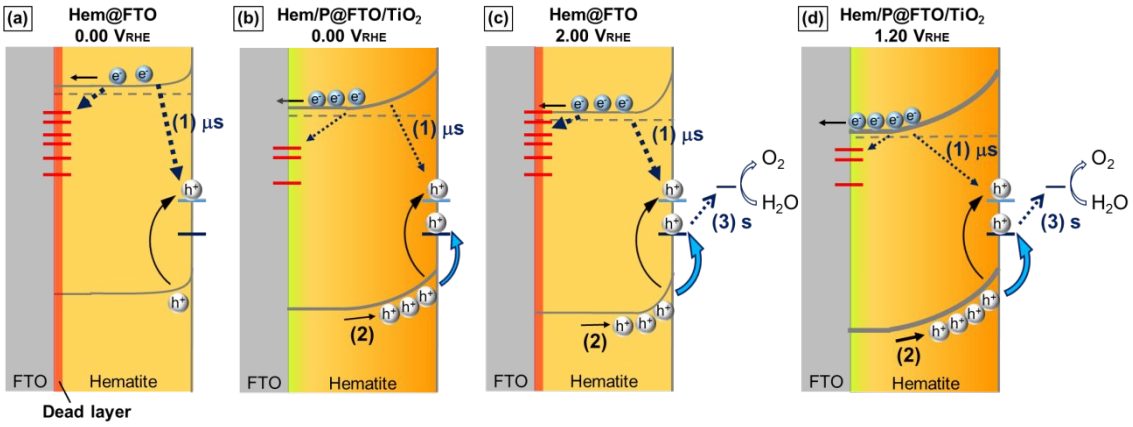


Figure 6 Schematic illustrations of the photo-generated charge carriers dynamics in (a) Hem@FTO at 0.00 $V_{RHE}$ and (c) 2.00 $V_{RHE}$ (b) Hem/P@FTO/$TiO_2$ at 0.00 $V_{RHE}$ and (d) 1.20 $V_{RHE}$

(1) Recombination arising from the surface trapped holes, (2) hole transport from the bulk to the surface and (3) charge transfer kinetics of the long-lived holes

recombination arising from the trapped holes was observed of which time constant was 120 ~ 340 µs (1). In Hem/P@FTO/$TiO_2$ shown in Figure 6b, because P surface doping with the concentration gradient profile produced the strong electric field in the hematite film, this resulted in the band bending even at 0 V vs RHE, which varied the space charge layer, giving rise to the generation of the long-lived holes even at 0 V vs RHE (2). In addition, because the $TiO_2$ underlayer removed the dead layer, the signal intensity in the response of Hem/P@FTO/$TiO_2$ strongly depended on the bias voltage

due to Fermi level unpinning, leading to the improvement of the charge separation efficiency under the bias condition. Then, the survived long-lived holes transferred to the electrolyte (3) resulted in the enhanced PEC performance with aids of the cooperative effects of the surface and interface treatments (Figure 6d).

On the other hands, in Hem@FTO, applying a high voltage was needed to generate the long-lived holes trapped at the surface states because Fermi level pinning resulting from the interface states in the dead layer obstructed the effective band bending. Thus, the intensity of the second component in the response of the bare hematite films under the bias condition was very weak and showed the voltage dependence very weakly (Figure 6c).

## 4. Conclusion

We successfully developed the hematite photo-anode possessing the tremendous advantages, unpinned Fermi level and the intrinsic depletion layer, resulting from the simultaneous treatments of the surface and the interface in the hematite film. In addition, we clearly revealed the role of each treatment in the physical and chemical properties of hematite and figured out the origin of the cooperative effect of these treatments on the performance by investigating the charge carrier dynamics using the time-resolved

spectroscopic technique. We believe that the simultaneous treatments in the surface and the interface, leading to the drastic improvement of the PEC performance, could be easily utilized in other nanostructured materials in the future and pave a road for developing new metal oxide photo-electrodes.

**Acknowledgement**

This research was financially supported by Grant-in-Aid for Takahashi Industrial and Economic Research Foundation, JST PRESTO (Grant No. JPMJPR1675), Institute of Science and Engineering, Chuo University, and The Science Research Promotion Fund from the Promotion and Mutual Aid Corporation for Private Schools of Japan.

**Reference**

1 A. Fujishima and K. Honda, *Nature*, 1972, **238**, 37–38.

2 T. W. Hamann, *Dalton Trans.*, 2012, **41**, 7830–7834.

3 X. Chen, S. Shen, L. Guo and S. S. Mao, *Chem. Rev.*, 2010, **110**, 6503–6570.

4 K. Sivula, F. Le Formal and M. Grätzel, *ChemSusChem*, 2011, **4**, 432–449.

5 J. H. Park, O. O. Park and S. Kim, *Appl. Phys. Lett.*, 2006, **89**, 163106.

6 C. Wang, Z. Chen, H. Jin, C. Cao, J. Li and Z. Mi, *J. Mater. Chem. A*, 2014, **2**, 17820–17827.

7 S. S. Dunkle, R. J. Helmich and K. S. Suslick, *J. Phys. Chem. C*, 2009, **113**, 11980–11983.

8 X. Chang, T. Wang, P. Zhang, J. Zhang, A. Li and J. Gong, *J. Am. Chem. Soc.*, 2015, **137**, 8356–8359.

9 T. W. Kim and K.-S. Choi, *Science*, 2014, **343**, 990–994.

10 C. Santato, M. Ulmann and J. Augustynski, *J. Phys. Chem. B*, 2001, **105**, 936–940.

11 M. Liu, C.-Y. Nam, C. T. Black, J. Kamcev and L. Zhang, *J. Phys. Chem. C*, 2013, **117**, 13396–13402.

12 F. Wang, C. Di Valentin and G. Pacchioni, *J. Phys. Chem. C*, 2012, **116**, 8901–8909.

13 J.-W. Jang, C. Du, Y. Ye, Y. Lin, X. Yao, J. Thorne, E. Liu, G. McMahon, J. Zhu, A. Javey, J. Guo and D. Wang, *Nat Commun*, 2015, **6**, 1–5.

14 J. Y. Kim, G. Magesh, D. H. Youn, J.-W. Jang, J. Kubota, K. Domen and J. S. Lee, *Sci Rep*, 2013, **3**, 2681.

15 J. H. Kennedy and K. W. Frese, *J. Electrochem. Soc.*, 1978, **125**, 723–726.

16 L. A. Marusak, R. Messier and W. B. White, *J. Phys. Chem. Sol.*, 1980, **41**, 981–984.

17 J. H. Kennedy and K. W. Frese, *J. Electrochem. Soc.*, 1978, **125**, 709–714.

18 S. Shen, S. A. Lindley, X. Chen and J. Z. Zhang, *Energy Environ. Sci.*, 2016, **9**, 2744–2775.

19 M. P. Dare-Edwards, J. B. Goodenough, A. Hamnett and P. R. Trevellick, *J. Chem. Soc., Faraday Trans. 1*, 1983, **79**, 2027–2041.

20 C. Du, M. Zhang, J.-W. Jang, Y. Liu, G.-Y. Liu and D. Wang, *J. Phys. Chem. C*, 2014, **118**, 17054–17059.

21 W. Y. Sohn, J. E. Thorne, Y. Zhang, S. Kuwahara, Q. Shen, D. Wang and K. Katayama, J. Photochem. Photobiol. A, 2018, **353**, 344–348.

22 H. Dotan, K. Sivula, M. Grätzel, A. Rothschild and S. C. Warren, *Energy Environ. Sci.*, 2011, **4**, 958–964.

23 M. Forster, R. J. Potter, Y. Ling, Y. Yang, D. R. Klug, Y. Li and A. J. Cowan, *Chem. Sci.*, 2015, **6**, 4009–4016.

24 F. Le Formal, E. Pastor, S. D. Tilley, C. A. Mesa, S. R. Pendlebury, M. Grätzel and J. R. Durrant, *J. Am. Chem. Soc.*, 2015, **137**, 6629–6637.

25 A. Kay, I. Cesar and M. Grätzel, *J. Am. Chem. Soc.*, 2006, **128**, 15714–15721.

26 C. Liu, N. P. Dasgupta and P. Yang, *Chem. Mater.*, 2014, **26**, 415–422.

27 Z. Luo, T. Wang, J. Zhang, C. Li, H. Li and J. Gong, Angew. Chem. Int. Ed, 2017, **56**, 12878–12882.

28 M. Barroso, C. A. Mesa, S. R. Pendlebury, A. J. Cowan, T. Hisatomi, K. Sivula, M. Grätzel, D. R. Klug and J. R. Durrant, *PNAS*, 2012, **109**, 15640–15645.

29 B. Klahr, S. Gimenez, F. Fabregat-Santiago, J. Bisquert and T. W. Hamann, *J. Am. Chem. Soc.*, 2012, **134**, 16693–16700.

30 D. K. Zhong, J. Sun, H. Inumaru and D. R. Gamelin, *J. Am. Chem. Soc.*, 2009, **131**, 6086–6087.

31 Y. Zhang, S. Jiang, W. Song, P. Zhou, H. Ji, W. Ma, W. Hao, C. Chen and J. Zhao, *Energy Environ. Sci.*, 2015, **8**, 1231–1236.

32 K. D. Malviya, D. Klotz, H. Dotan, D. Shlenkevich, A. Tsyganok, H. Mor and A. Rothschild, *J. Phys. Chem. C*, 2017, **121**, 4206–4213.

33 P. Liao, M. C. Toroker and E. A. Carter, *Nano Lett.*, 2011, **11**, 1775–1781.

34 Y. Ling, G. Wang, D. A. Wheeler, J. Z. Zhang and Y. Li, *Nano Lett.*, 2011, **11**, 2119–2125.

35 K. M. Rosso, D. M. A. Smith and M. Dupuis, *J. Chem. Phys.*, 2003, **118**, 6455.

36 S. Sreekantan, S. Mohd. Zaki, C. W. Lai and T. W. Tzu, *Materials Science in Semiconductor Processing*, 2014, **26**, 620–631.

37 J. Zhu, Z. Deng, F. Chen, J. Zhang, H. Chen, M. Anpo, J. Huang and L. Zhang, *Appl. Catal. B*, 2006, **62**, 329–335.

38 S. P. Jiang, Mat. Sci. Eng. A, 2006, **418**, 199–210.

39 Z. Luo, C. Li, S. Liu, T. Wang and J. Gong, *Chem. Sci.*, 2016, **8**, 91–100.

40 J. Zou, Z. Yang, J. Qiao, P. Gao and B. Chang, in *Optoelectronic Materials and Devices II*, International Society for Optics and Photonics, 2007, vol. 6782, p. 67822R.

41 T. Hisatomi, H. Dotan, M. Stefik, K. Sivula, A. Rothschild, M. Grätzel and N. Mathews, Adv. Mater., 2012, **24**, 2699–2702.

42 T. Hisatomi, J. Brillet, M. Cornuz, F. Le Formal, N. Tétreault, K. Sivula and M. Grätzel, *Faraday Discuss.*, 2012, **155**, 223–232; discussion 297-308.

43 F. L. Souza, K. P. Lopes, E. Longo and E. R. Leite, *Phys. Chem. Chem. Phys.*, 2009, **11**, 1215–1219.

44 C. Li, Z. Luo, T. Wang and J. Gong, *Adv. Mater.*, 2018, **30**, 1707502.

45 A. Subramanian, A. Annamalai, H. H. Lee, S. H. Choi, J. Ryu, J. H. Park and J. S. Jang, *ACS Appl. Mater. Interfaces*, 2016, **8**, 19428–19437.

46 L. Steier, I. Herraiz-Cardona, S. Gimenez, F. Fabregat-Santiago, J. Bisquert, S. D. Tilley and M. Grätzel, *Adv. Funct. Mater.*, 2014, **24**, 7681–7688.

47 A. Annamalai, P. S. Shinde, A. Subramanian, J. Y. Kim, J. H. Kim, S. H. Choi, J. S. Lee and J. S. Jang, *J. Mater. Chem. A*, 2015, **3**, 5007–5013.

48 J. W. Park, M. A. Mahadik, H. Ma, G. W. An, H. H. Lee, S. H. Choi, W.-S. Chae,

H.-S. Chung and J. S. Jang, *ACS Sustainable Chem. Eng.*, 2019, **7**, 6947–6958.

49 M. Inaba, J. E. Thorne, D. Wang, W. Y. Sohn and K. Katayama, J. Photochem. Photobiol., 2018, **364**, 645–649.

50 W. Y. Sohn, M. Inaba, T. Tokubuchi, J. E. Thorne, D. Wang and K. Katayama, *J. Phys. Chem. C*, 2019, **123**, 6693–6700.

51 T. H. Jeon, G. Moon, H. Park and W. Choi, *Nano Energy*, 2017, **39**, 211–218.

52 W. Y. Sohn, S. Kuwahara, J. E. Thorne, D. Wang and K. Katayama, *ACS Omega*, 2017, **2**, 1031–1035.

53 D. Shingai, Y. Ide, W. Y. Sohn and K. Katayama, *Phys. Chem. Chem. Phys.*, 2018, **20**, 3484–3489.

54 S. Kuwahara and K. Katayama, *Phys. Chem. Chem. Phys.*, 2016, **18**, 25271–25276.

55 J. A. Venables, G. D. T. Spiller and M. Hanbucken, *Rep. Prog. Phys.*, 1984, **47**, 399–459.

56 X. Y. Meng, G. W. Qin, S. Li, X. H. Wen, Y. P. Ren, W. L. Pei and L. Zuo, *Appl. Phys. Lett.*, 2011, **98**, 112104.

57 X. Wang, W. Gao, Z. Zhao, L. Zhao, J. P. Claverie, X. Zhang, J. Wang, H. Liu and Y. Sang, *Appl. Catal., B*, 2019, **248**, 388–393.

58 S. George, S. Pokhrel, Z. Ji, B. L. Henderson, T. Xia, L. Li, J. I. Zink, A. E. Nel and

L. Mädler, *J. Am. Chem. Soc.*, 2011, **133**, 11270–11278.

59 Y. Yang, Y. Yu, J. Wang, W. Zheng and Y. Cao, *CrystEngComm*, 2017, **19**, 1100–1105.

60 M. M. Momeni and Y. Ghayeb, *J. Electroanal. Chem.*, 2015, **751**, 43–48.

61 D. P. Jaihindh, A. Verma, C.-C. Chen, Y.-C. Huang, C.-L. Dong and Y.-P. Fu, *Int. J. Hydrog. Energy*, 2019, **44**, 15892–15906.

62 M. Barroso, S. R. Pendlebury, A. J. Cowan and J. R. Durrant, *Chem. Sci.*, 2013, **4**, 2724–2734.

63 P. J. Steinbach, *Anal. Biochem.*, 2012, **427**, 102–105.

64 M. Barroso, C. A. Mesa, S. R. Pendlebury, A. J. Cowan, T. Hisatomi, K. Sivula, M. Grätzel, D. R. Klug and J. R. Durrant, *PNAS*, 2012, **109**, 15640–15645.

65 O. Zandi, B. M. Klahr and T. W. Hamann, *Energy Environ. Sci.*, 2013, **6**, 634–642.

**TOC**